Supporting Information

Ion irradiation to control size, composition and dispersion of metal nanoparticle exsolution

Jiayue Wang[1], Kevin B. Woller[1], Abinash Kumar[2], Zhan Zhang[3], Hua Zhou[3], Iradwikanari Waluyo[4], Adrian Hunt[4], James M. LeBeau[2], Bilge Yildiz[1,2*]

[1]Department of Nuclear Science and Engineering, Massachusetts Institute of Technology, Cambridge, MA 02139, USA

[2]Department of Materials Science and Engineering, Massachusetts Institute of Technology, Cambridge, MA 02139, USA

[3]Advanced Photon Source, Argonne National Laboratory, Lemont, IL 60439, USA

[4]National Synchrotron Light Source II, Brookhaven National Laboratory, Upton, NY 11973, USA

* e-mail: byildiz@mit.edu

Supplementary Table S1: Summary of exsolution tuning in literature

Host Oxide*	Tuning method	Tailored property	Particle size	Ref.
$La_{0.2}Sr_{0.7}Ti_{0.9}Ni_{0.1}O_3$	Strain	Size, density	5 nm	[1]
$La_{0.43}Ca_{0.37}Ti_{0.94}Ni_{0.06}O_3$	Plasma	Size, density	11 nm	[2]
$La_{0.43}Ca_{0.37}Ti_{0.94}Ni_{0.06}O_3$	Plasma	Size, density	20 nm	[3]
$La_{0.43}Ca_{0.37}Ti_{0.94}Ni_{0.06}O_3$	Thermal shock	Size, density	14 nm	[4]
$La_{0.43}Ca_{0.37}Ti_{0.94}Ni_{0.06}O_3$	Voltage	Size, density	15 nm	[5]
$La_{0.6}Sr_{0.4}FeO_3$	Voltage	Size, density	55 nm	[6]
$La_{0.4}Ca_{0.4}Ti_{0.88}Fe_{0.06}Ni_{0.06}O_3$	Voltage	Size, density	30 nm	[7]
$Pr_{0.5}Ba_{0.2}Sr_{0.3}FeO_3$	Oxide composition	Size, density	150 nm	[8]
$La_{0.4}Sr_{0.6}Ti_{0.6}Fe_{0.35}Ni_{0.05}O_3$	Oxide composition	Composition	10 nm	[9]
$SrTi_{0.9}Nb_{0.05}Ni_{0.05}O_3$	Oxide composition	Size, density	30 nm	[10]
$La_{2-x}NiRuO_6$	Oxide composition	Size, density	2-6 nm	[11]
$SrFe_{1-2x}Ni_xMo_xO_3$	Oxide composition	Size, density	20 nm	[12]
$La_{0.9}Ca_{0.1}Fe_{1-x}Ni_xO_3$	Oxide composition	Size, density	8–30 nm	[13]
$La_{0.4}Sr_{0.4}Ti_{0.9}Cu_{0.1}O_3$	Oxide composition	Size, density	3 nm	[14]
$SrFe_{0.85}Ti_{0.1}Ni_{0.05}O_3$	Photochemistry	Size, density	20 nm	[15]
Pt-WO_3	Photothermal	Size, density	5 nm	[16]
$PrBaMn_{1.7}Co_{0.3}O_5$	Surface coating (cation swap)	Composition, density	30 nm	[17]
$Sr_{0.98}Ti_{0.95}Co_{0.05}O_3$	Reducing condition	Size, density	3-6 nm	[18]
$Sr_xFeCo_{0.2}Ni_{0.2}Mn_{0.1}Mo_{0.5}O_6$	Reducing condition, oxide composition	Composition, size, density	10 – 30 nm	[19]
$Sr_2Fe_{1.4}Ru_{0.1}Mo_{0.5}O_6$	Redox manipulation	Size, density	2-3 nm	[20]

* The to-be-exsolved cations are highlighted in red.

Supplementary Figures

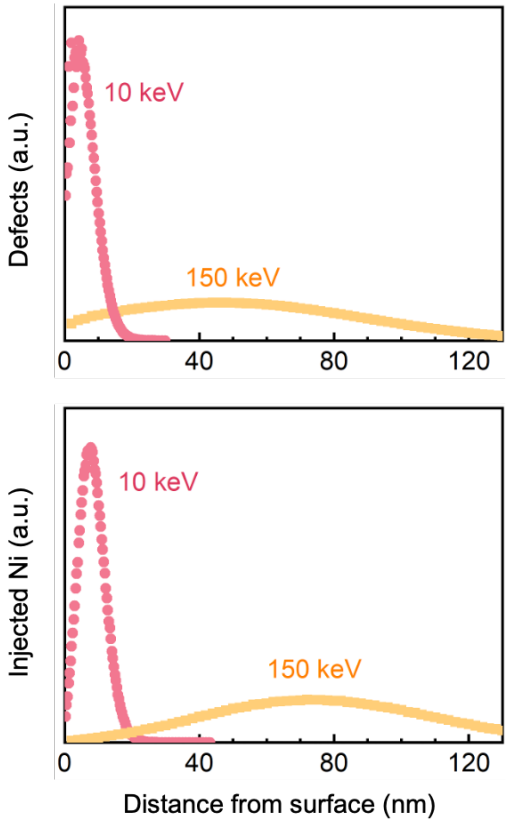

Figure S1. Energy-dependent ion-matter interactions. SRIM-simulated profiles of the Ni beam induced defects (top) and the injected Ni along the irradiation direction (bottom) in $SrTiO_3$ for both 10 and 150 keV Ni ions. Note the ion-matter interactions from 10 keV Ni is more surface-sensitive than that of 150 keV Ni. In the SRIM simulation, we considered normal ion impingement.

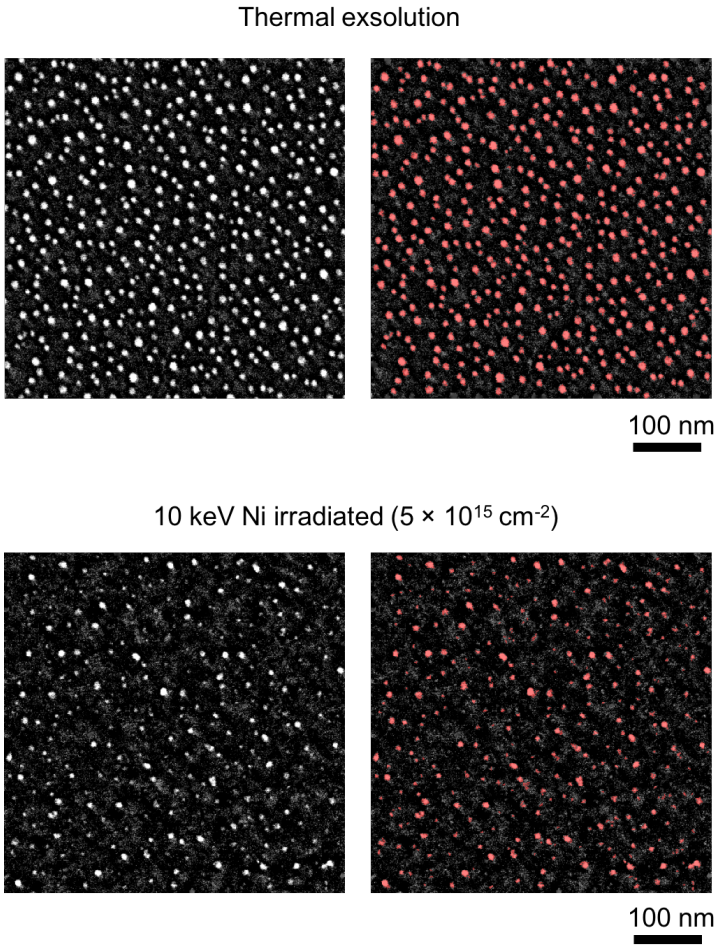

Figure S2. Representative particle analysis results. The SEM images are analyzed using the Gwyddion software[21]. The marked nanoparticles are highlighted in red.

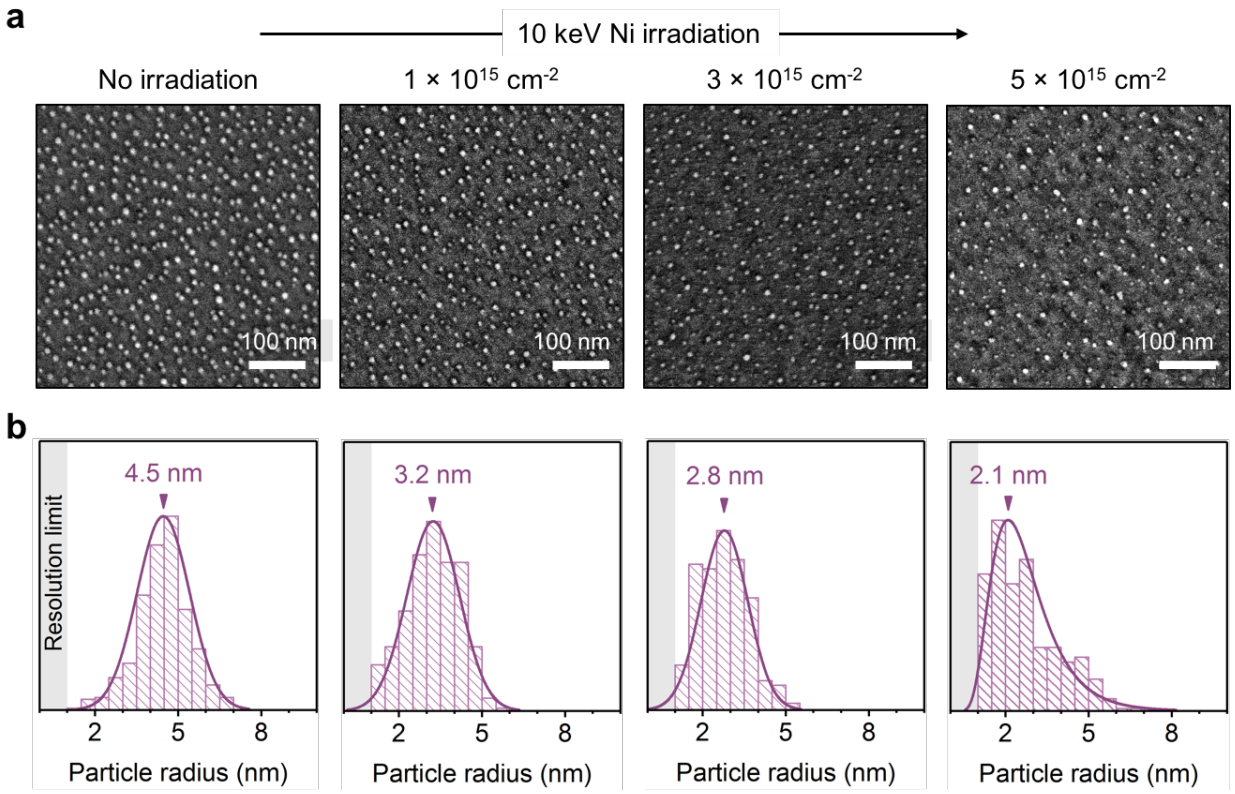

Figure S3. Supporting SEM images and particle size histograms for Figure 2d in the main text. (a) SEM images showing the morphologies of the exsolved STF surfaces under different doses of 10 keV Ni irradiation. **(b)** Histogram of the particle radius of the corresponding SEM images in plot (a), where the mode values of the particle radii are highlighted with arrows.

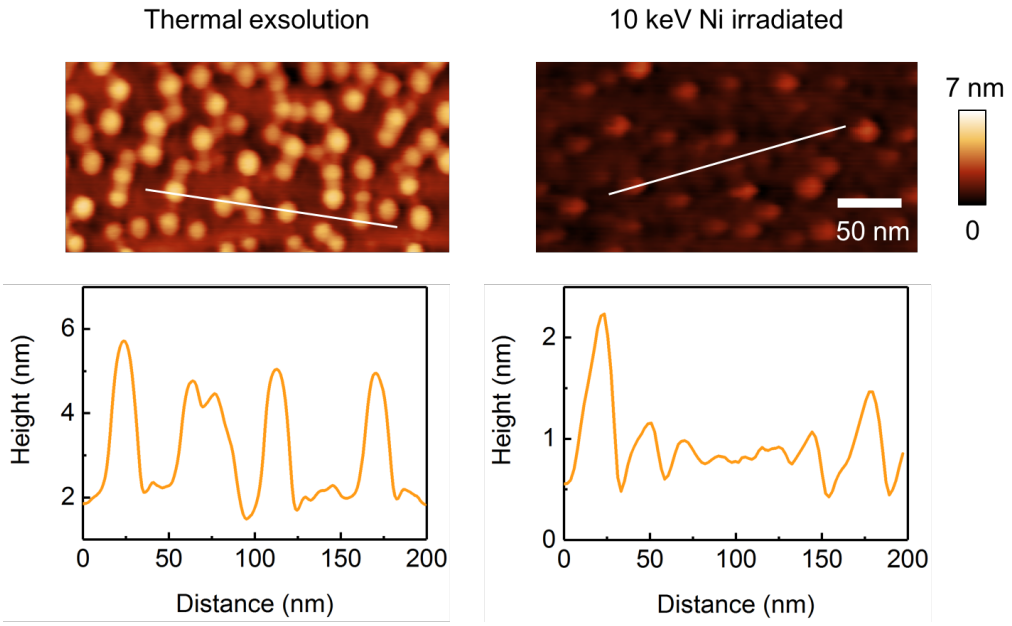

Figure S4. Ion beam irradiation reduces the particle height. *Ex-situ* AFM images together with the line profile showing the surface morphologies of the thermally exsolved and 10 keV Ni-irradiated STF film. Note that the particle height on the Ni irradiated sample is much smaller than the thermally exsolved sample. The ion fluence for the 10 KeV Ni irradiation is 5×10^{15} cm^{-2}.

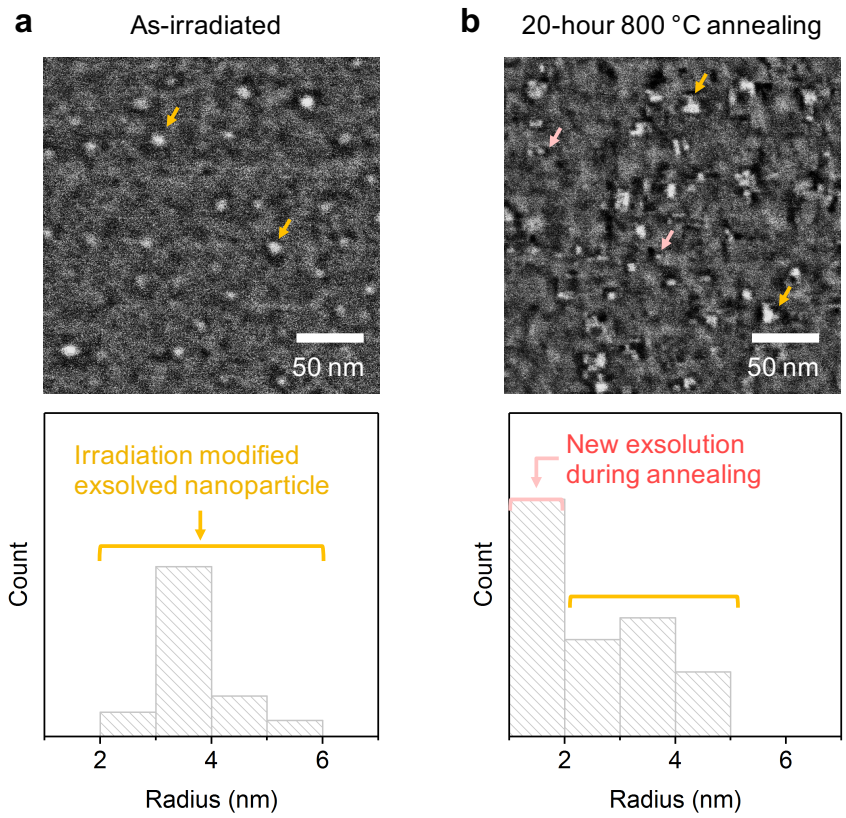

Figure S5. Thermal stability of the irradiation-modified exsolved nanoparticles. *Ex-situ* SEM images and the corresponding histograms of the **(a)** as-irradiated STF and **(b)** after 20-hour annealing at 800 °C in 5:3 H_2/H_2O atmosphere, with a gas flow rate of 90 sccm and a ramping rate of 5 °C/min. Note that no significant particle growth can be observed after the thermal annealing test (indicated by the yellow arrows), indicating high particle thermal stability. More interestingly, some additional nanoparticles appeared on the surface (indicated by the pink arrows) after the annealing, which is due to the newly exsolved nanoparticles. The irradiation condition is 5×10^{15} cm^{-2}, 20 keV Ni irradiation.

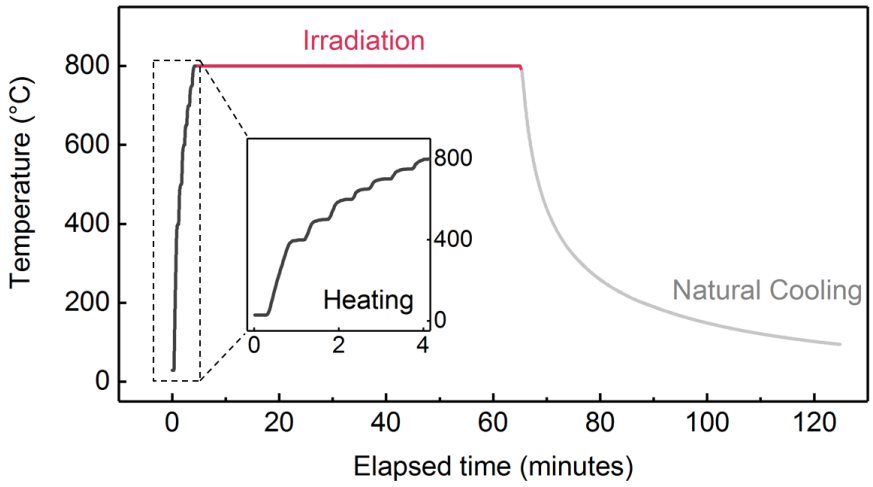

Figure S6. Sample temperature profile during the irradiation experiment. For the irradiation-assisted exsolution, the sample is rapidly heat up to 800 °C (roughly 200 °C/min) and undergoes 1-hour irradiation at 800 °C before cooling down. For the thermally exsolved sample, the temperature profile is exactly the same, just without irradiation.

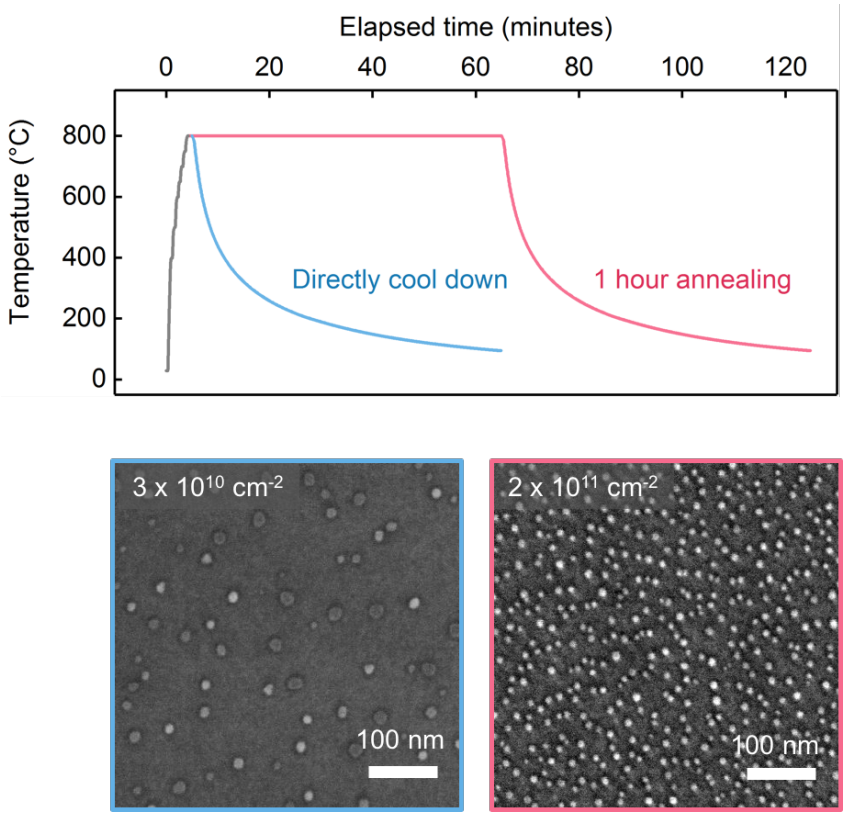

Figure S7. The majority of the nanoparticles are exsolved during the annealing step. The purpose of using rapid heating is to ensure that most of the exsolved nanoparticles are nucleated during the annealing/irradiation stage, rather than during the temperature ramping period. To confirm that the majority of nanoparticles exsolve during the annealing/irradiation stage, we prepared two samples. The first sample (blue) was immediately cool down after reaching 800 °C, while the second sample (red) underwent standard heating procedure (described in Figure S6). As illustrated in the *ex-situ* SEM images, the particle density on the standard sample (red) is almost one order of magnitude higher than that of the immediately cooled sample. This indicates that most of the nanoparticles are nucleated after the sample has reached 800 °C, i.e., during the annealing step.

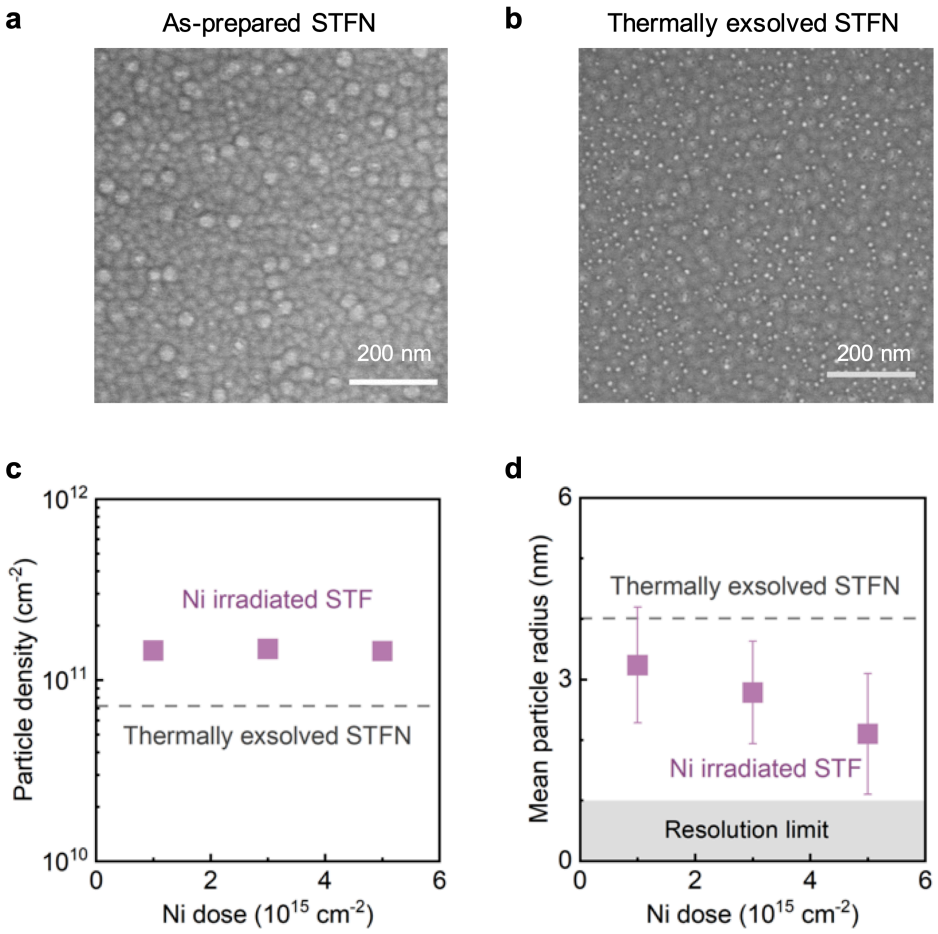

Figure S8. Thermal exsolution characteristics of Ni-doped STF films. (a-b) SEM images of $SrTi_{0.65}Fe_{0.3}Ni_{0.05}O_3$ (STFN) thin films, captured (a) before and after (b) thermal exsolution. **(c-d)** Comparative analysis of the (c) particle density and (d) average particle size between the thermally exsolved STFN film and the Ni-irradiated STF film. Notably, Ni-irradiated STF demonstrates the capability to produce finer and denser exsolved nanoparticles in contrast to those generated through thermal exsolution in STFN. The thermal exsolution condition for STFN is described in Figure S6.

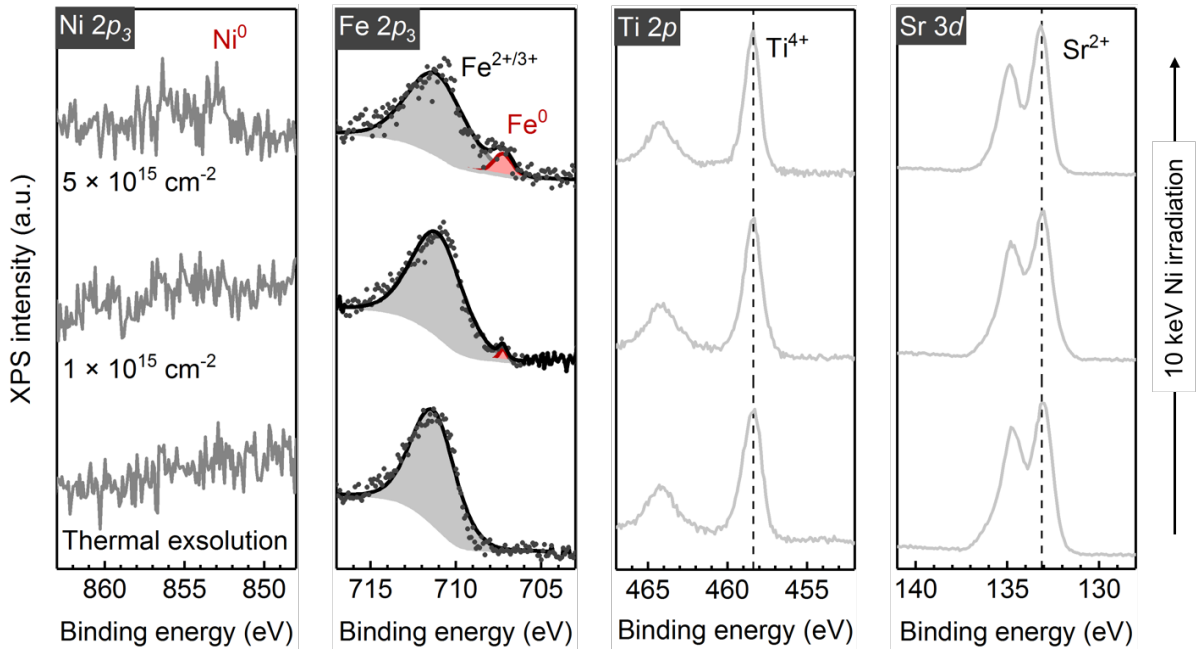

Figure S9. Core-level XPS measurements of the STF films as a function of 10 keV Ni irradiation dose. Note the appearance of Ni^0 and Fe^0 with increasing Ni irradiation. Meanwhile, Ti and Sr spectra remained largely invariant. All the spectra are calibrated by aligning the Ti $2p_{3/2}$ peak to 458.4 eV.

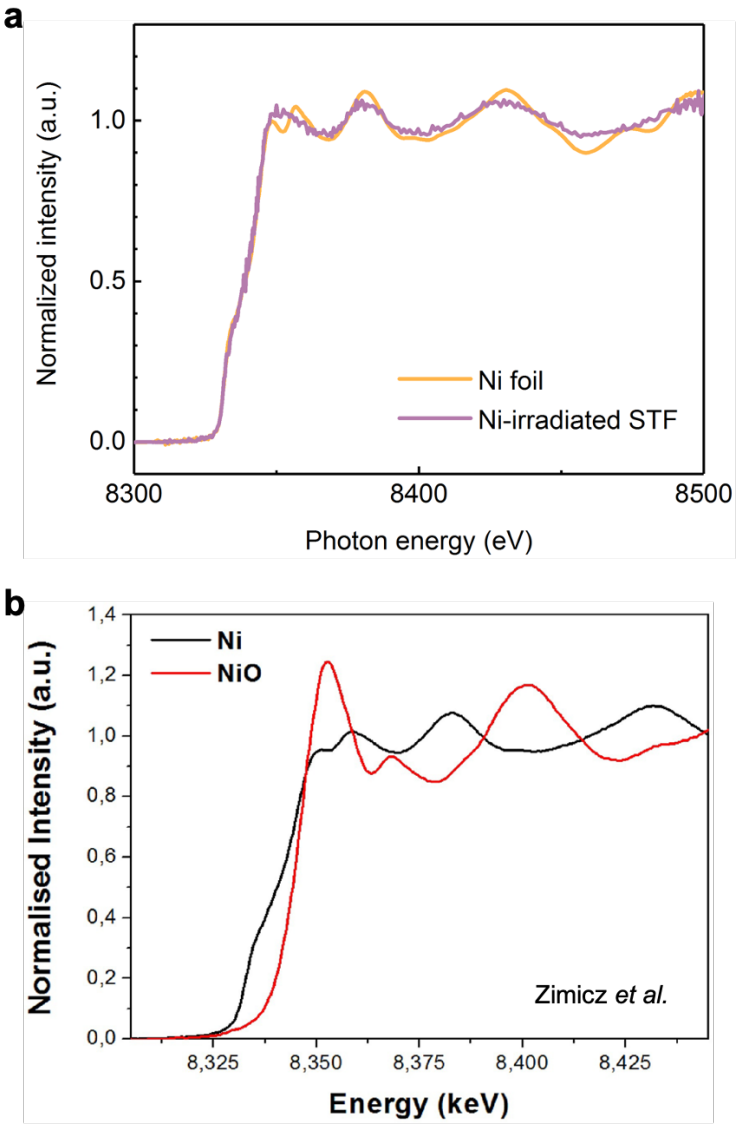

Figure S10. Ni K-edge X-ray absorption spectra of 10 keV Ni-irradiated STF film. (a) Comparison of Ni K-edge spectra between metallic Ni foil and Ni-irradiated STF film. Note that the pre-edge features in both samples overlap very well, which implies that the implanted Ni species in the 10 keV Ni-irradiated STF is primarily in the metallic state (i.e., Ni^0). The Ni irradiation dose is 5×10^{15} cm^{-2}. **(b)** Reference Ni K-edge spectra for Ni and NiO standards, adapted from Ref. [22]. Note that the NiO (Ni^{2+}) can have distinct pre-edge features than metallic Ni (Ni^0). We also note that in the extended energy region (E > 8350 eV), the Ni-irradiated STF exhibit different features than the Ni foil. This difference suggests that the implanted Ni has a different local atomic environment compared to that of the Ni foil. This can be expected, and attributed to two factors. First, as revealed by the GIXRD data in Figure 4 in the main text, the implanted Ni leads to the formation of Ni-Fe alloy, whose atomic configuration can differ from that of pure Ni[23]. Secondly, considering that the implanted Ni is embedded within an oxide matrix, the coordination environment of Ni could also deviate from that found in pristine Ni metal.

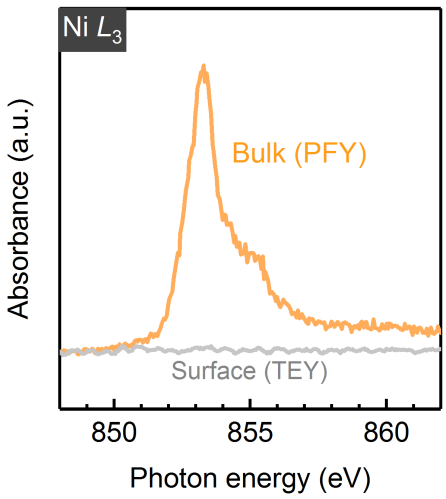

Figure S11. X-ray absorption spectroscopy (XAS) showing the different surface and bulk chemistry in 150 Ni-irradiated STF film. Note that Ni signal can be only detected using bulk-sensitive, partial fluorescence yield (PFY) mode XAS. On the other hand, surface-sensitive, total electron yield (TEY) mode XAS confirms that negligible Ni is present in the near-surface region. The Ni dose is 5×10^{15} cm^{-2}.

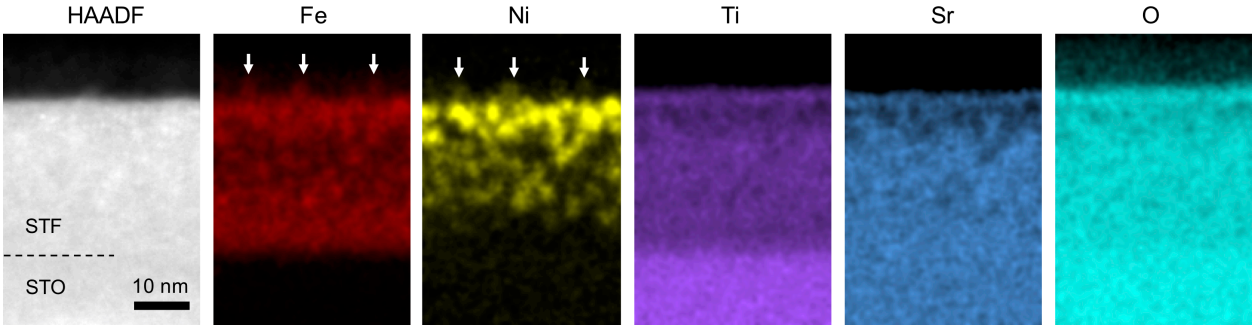

Figure S12. HAADF-STEM image and EDX maps of the 10 keV Ni irradiated STF film. The locations of the exsolved nanoparticles are highlighted with arrows. Note that the surface nanoparticles are enriched in Fe and Ni, while depleted in Ti and Sr. The Ni dose is 5×10^{15} cm^{-2}. The color intensities represent the atomic concentrations.

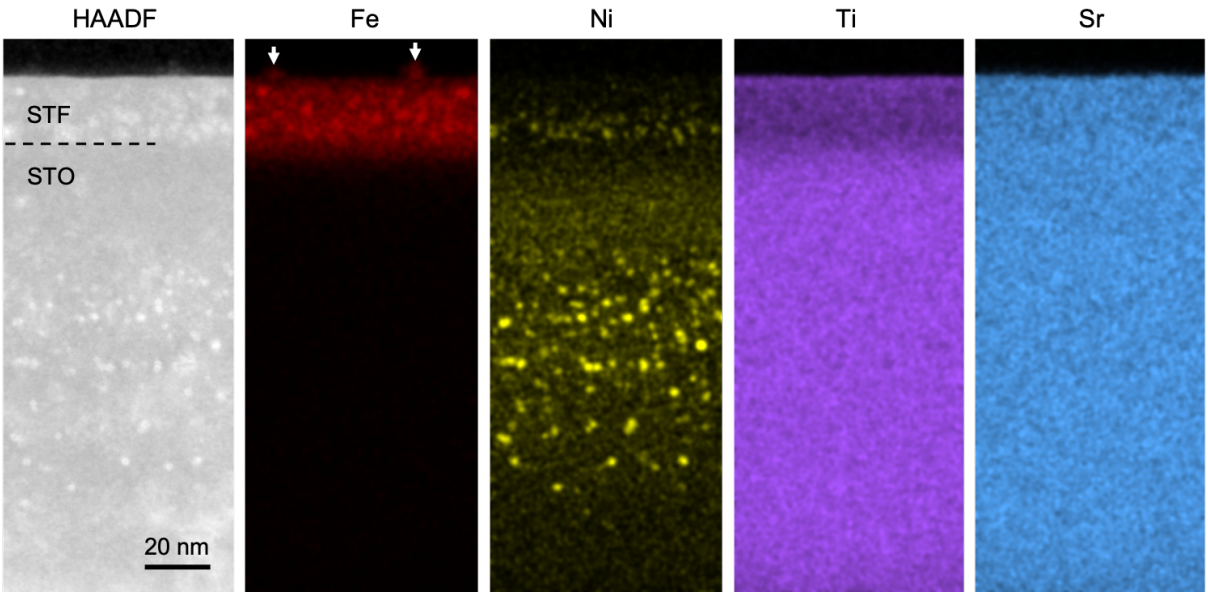

Figure S13. HAADF-STEM image and the corresponding EDX maps of the 150 keV Ni irradiated STF film. The surface exsolved nanoparticles are highlighted with arrows. Note that the surface nanoparticles are enriched in Fe, while depleted in Ni, Ti and Sr. The Ni dose is 5×10^{15} cm^{-2}. In particular, no significant Ni signals can be found near the STF surface. Rather, strong Ni intensities are observed in the STO substrate. The color intensities represent the atomic concentrations.

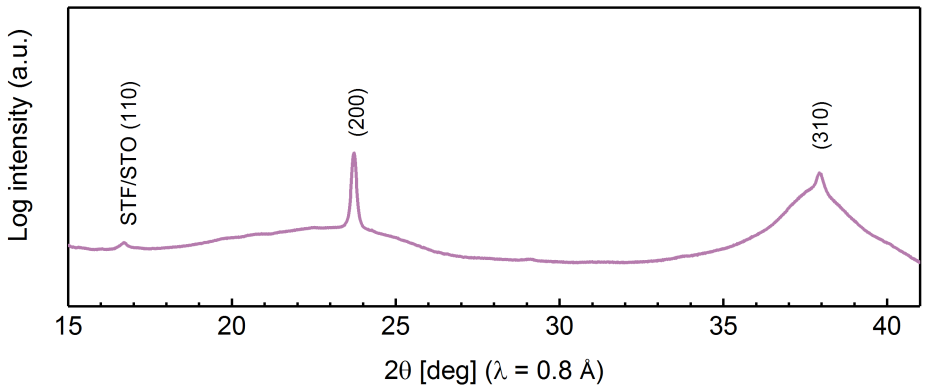

Figure 14. GID pattern of the as-prepared STF film. As illustrated, no metal diffraction can be observed on the as-prepared STF film. The incident angle is 0.09 deg.

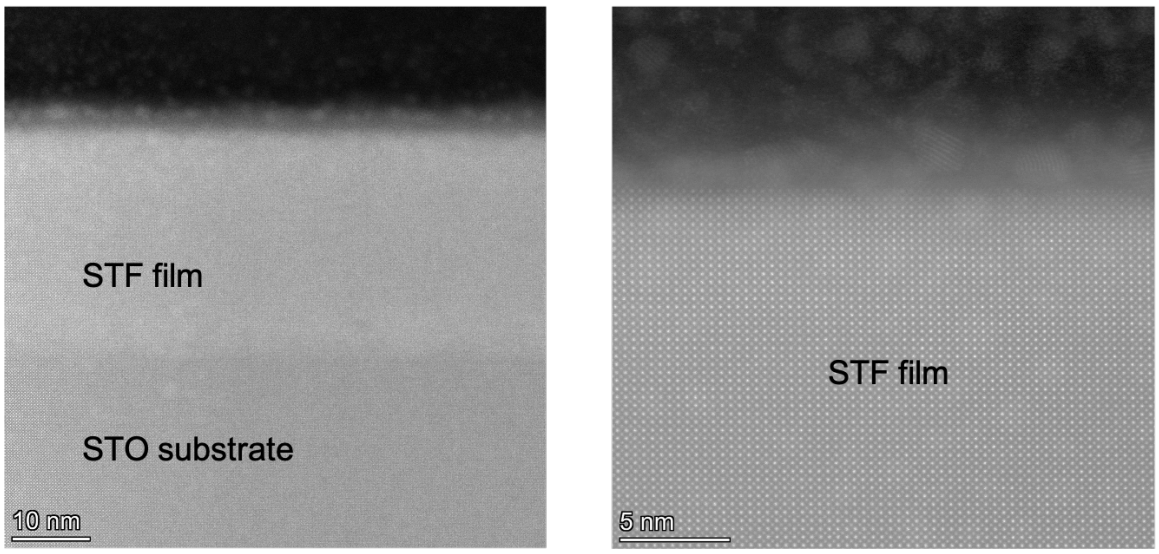

Figure S15. High-resolution HAADF-STEM images of the thermally exsolved STF film. Note that no bulk exsolution can be observed in the sub-surface region in the sample.

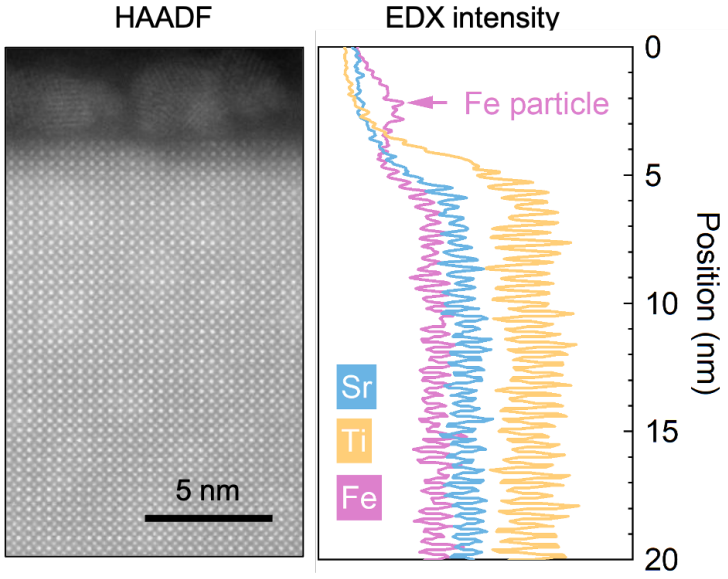

Figure S16. Chemical homogeneity of the thermally exsolved STF film. Atomically resolved EDS shows that the thermally exsolved STF film has uniform chemistry in the sub-surface region.

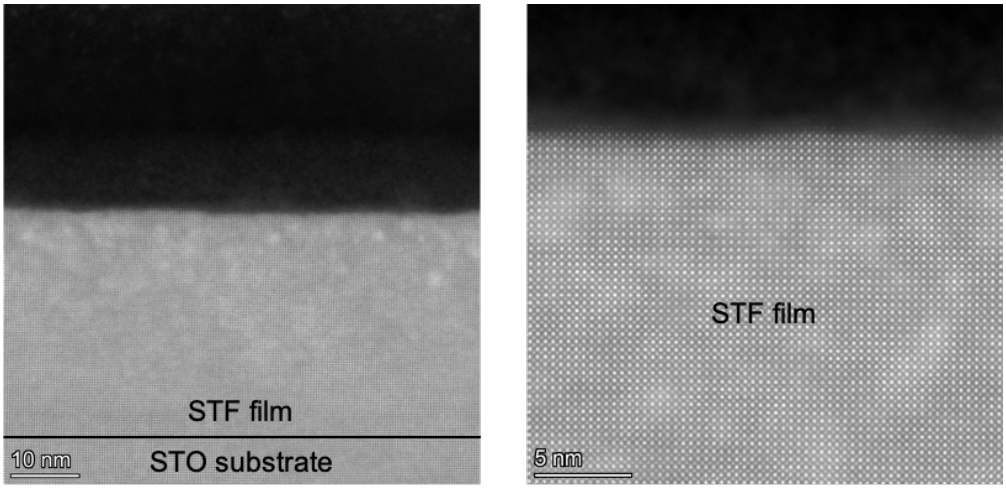

Figure S17. High-resolution HAADF-STEM images of the 10 keV Ni-irradiated STF film (dose: 5×10^{15} cm^{-2}). Note that contrasts can be observed in the sub-surface of the STF film.

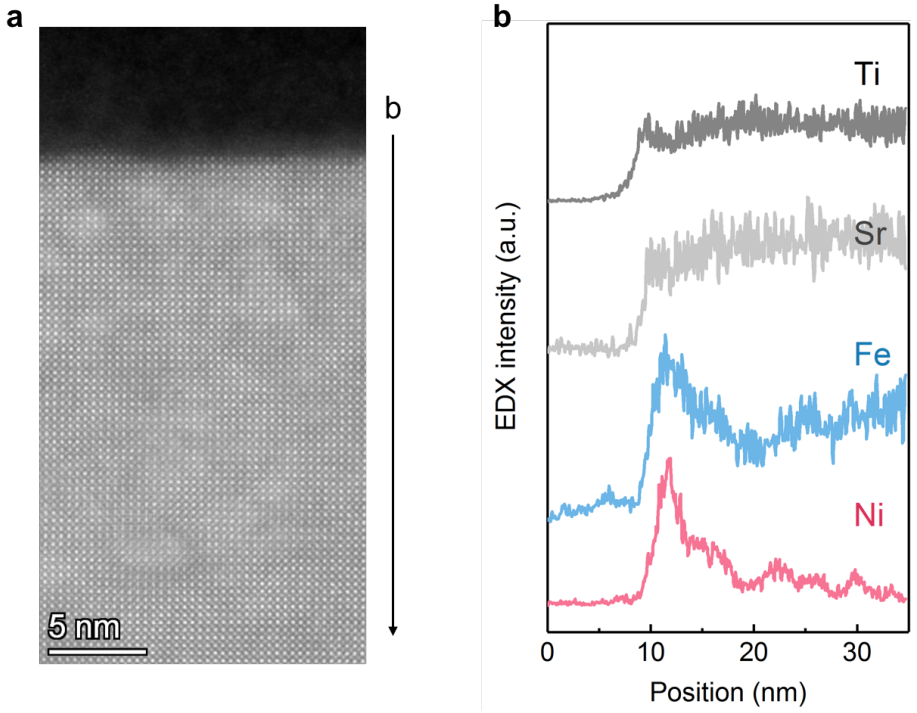

Figure S18. Sub-surface chemical inhomogeneity in the 10 keV Ni irradiated STF film (dose: 5×10^{15} cm^{-2}). **(a)** HAADF-STEM image and **(b)** EDX line profile of the 10 keV Ni irradiated STF film. The EDX profiling direction is highlighted in plot (a). The EDX line profiles are displaced vertically for better visualization. Note that the near-surface region is enriched in both Ni and Fe, which is significantly different from the thermal exsolution case (Figure S13). This observation indicates that Ni implantation also facilitates the segregation and precipitation of Fe in bulk STF.

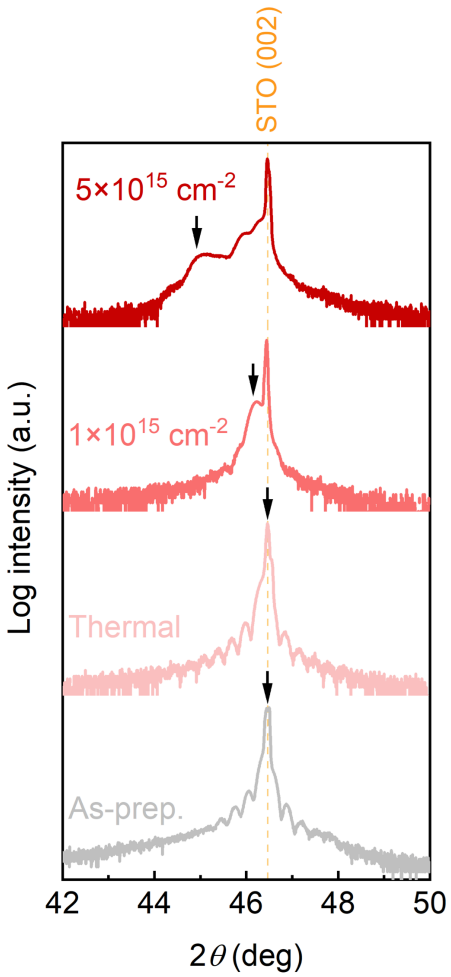

Figure S19. Out-of-plane XRD scans in STF film at different irradiation and exsolution conditions. The position of the STF (002) peak is highlighted with arrows. As illustrated, the STF peak shifts toward lower 2 theta values upon 10 keV Ni irradiation, which suggests that Ni irradiation induces out-of-plane lattice expansion in the STF film. This can be a combination of irradiation-induced point defect formation in STF, and due to the lattice strain induced by the embedded metal nanoparticles in STF.

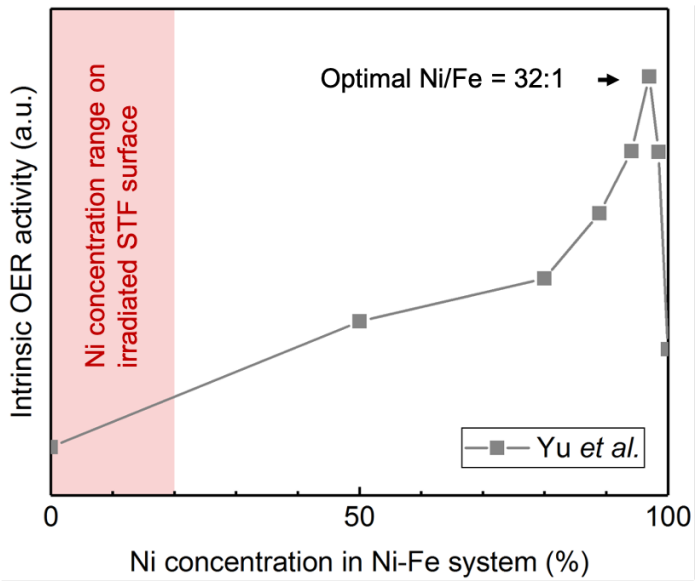

Figure S20. OER activity of the Ni-Fe system as a function of Ni/Fe ratio. The data points are replotted from Ref. [23]. As illustrated, the maximum OER activity was obtained with a Ni concentration of 97% (i.e., a Ni/Fe ratio of 32/1). The shaded region on the graph represents the range of surface Ni concentrations observed on irradiated STF, as quantified through XPS (see Figure S9). It's important to note that the maximum Ni concentration reached in this study is approximately 0.2, significantly lower than the optimal Ni concentration for achieving maximum OER activity. Therefore, we expect that for our experimental conditions, the intrinsic activity of surface Ni-Fe alloy nanoparticle should monotonically increase with Ni irradiation dose.

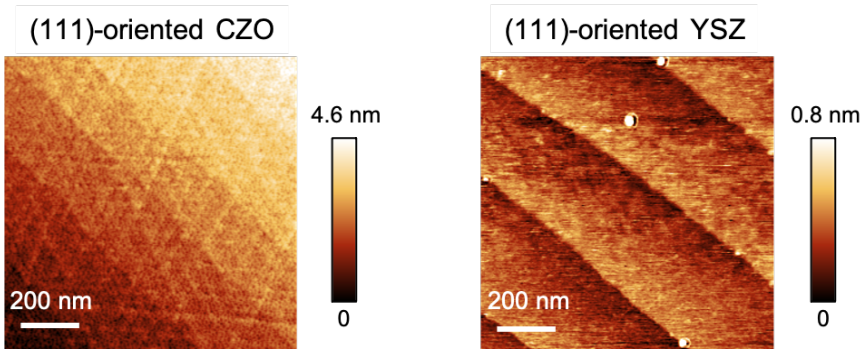

Figure S21. Smooth surfaces of CZO and YSZ before ion irradiation. AFM images showing the surface morphology of as-prepared CZO film and YSZ single crystals.

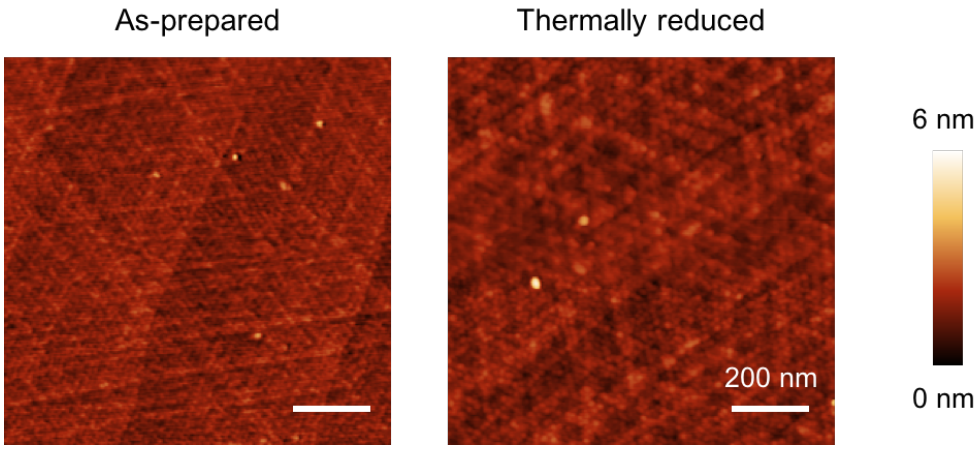

Figure S22. Effect of thermal reduction on the ceria surface morphology. The thermal reduction was conducted by annealing the CZO film in 5% H_2/N_2 atmosphere at 800 °C for 2 hours, with a ramp rate of 5 °C/min. As illustrated, thermal reduction alone would not generate the surface nanoparticles. The sparse bright features in the AFM images are surface defects.

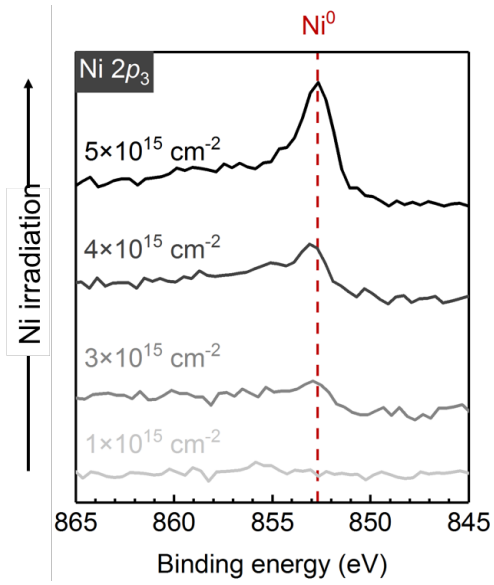

Figure S23. Effect of Ni irradiation in tailoring the surface chemistry of the CZO film. As illustrated by the *ex-situ* XPS spectra, the concentration of metallic Ni (Ni^0) species in the near surface region of CZO increased with prolonged Ni irradiation.

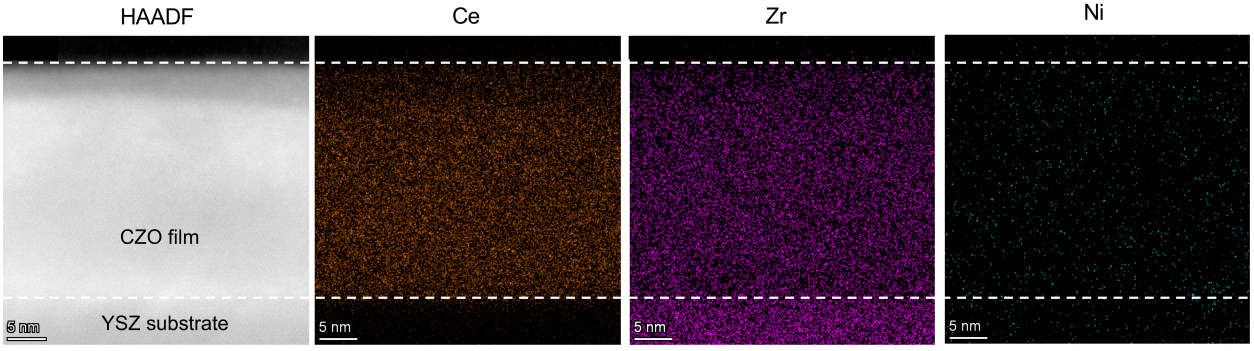

Figure S24. HAADF-STEM image and EDX chemical maps of a 10 keV Ni-irradiated CZO film (dose: 1×10^{15} cm^{-2}). Notably, there is no observable surface precipitation of Ce and Zr. Detection of the Ni signal is challenging due to its low concentration and the limited size of exsolved nanoparticles present in the sample.

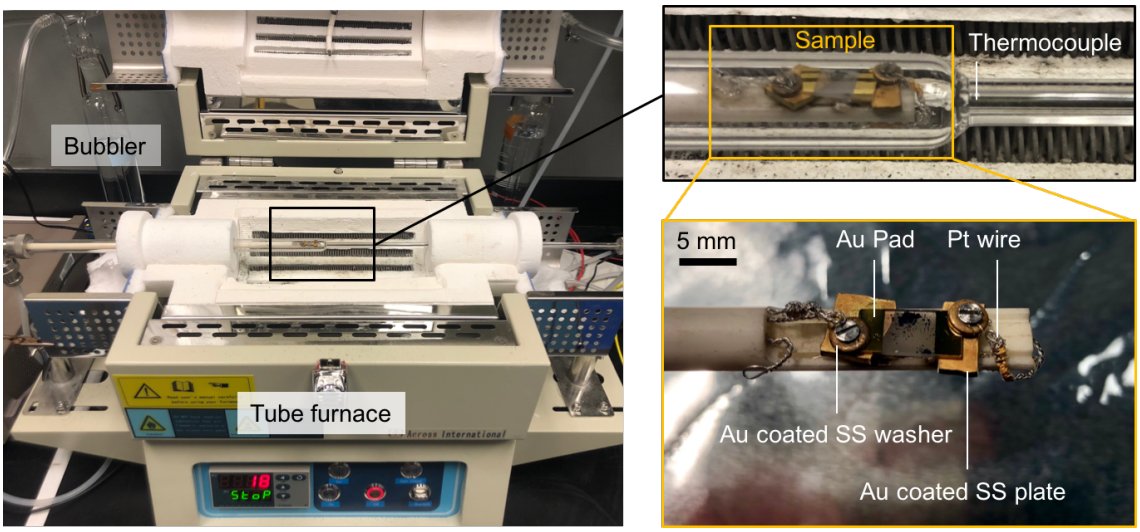

Figure S25. Experimental setup for the electrical conductivity relaxation (ECR) measurements. The ECR measurements were made in an in-house constructed ECR reactor with a sample chamber volume of approximately 1.25 cm^3. The small chamber volume ensured rapid changes in pO_2. The targeted pO_2 values were obtained by adjusting the gas mixtures of H_2–H_2O–N_2, with a total gas flow rate of 400 sccm. In all cases, the pH_2O was fixed to be 0.023 atm by passing pre-mixed N_2 and H_2 gases through a water bubbler at room temperature. To avoid potential contamination from the paint, Au coated stainless steel ("SS") screws were employed to mount and contact the sample. Two gold (Au) electrodes (100 nm-thick and 5 mm-distance) were deposited onto the film surface via DC magnetron sputtering as current collectors. The in-plane sample conductivity was measured with a Keithley 2461 Sourcemeter at an applied DC voltage of 100 mV.

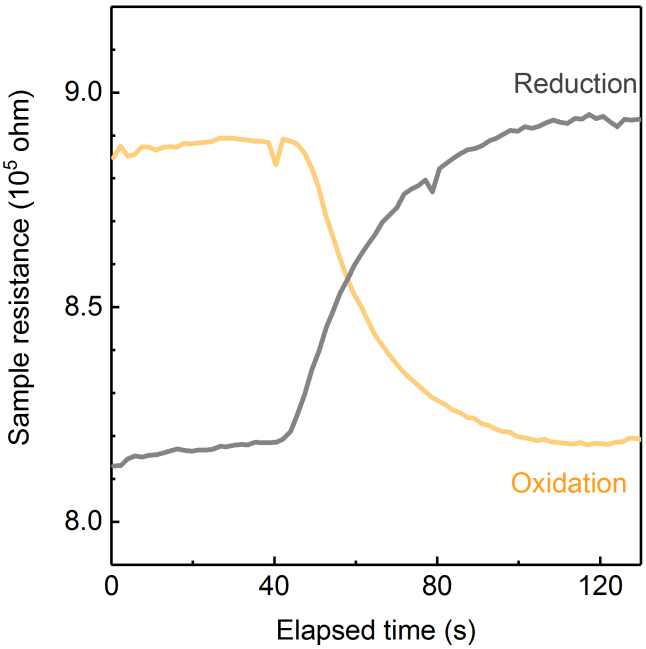

Figure S26. Raw conductivity relaxation profiles along the reducing and oxidizing directions. The ECR measurements were conducted both in the oxidation and reduction directions to confirm that the pO_2 step change was small enough to justify the assumptions of first order surface reaction kinetics[24]. The pO_2 switch is between 1.4×10^{-32} atm and 3.9×10^{-32} atm, and the temperature is at 400 °C. The normalized conductivity as a function of time was fitted to the following equation[24] to obtain the surface exchange coefficients (k_s): $\frac{\sigma(t)-\sigma(0)}{\sigma(t)-\sigma(\infty)} = 1 - exp\left(\frac{k_s t}{a}\right)$, where t denotes the elapsed time after the pO_2 change, and $\sigma(0)$ and $\sigma(\infty)$ are the initial and final conductivities of the sample, respectively. In addition, a represents the film thickness.

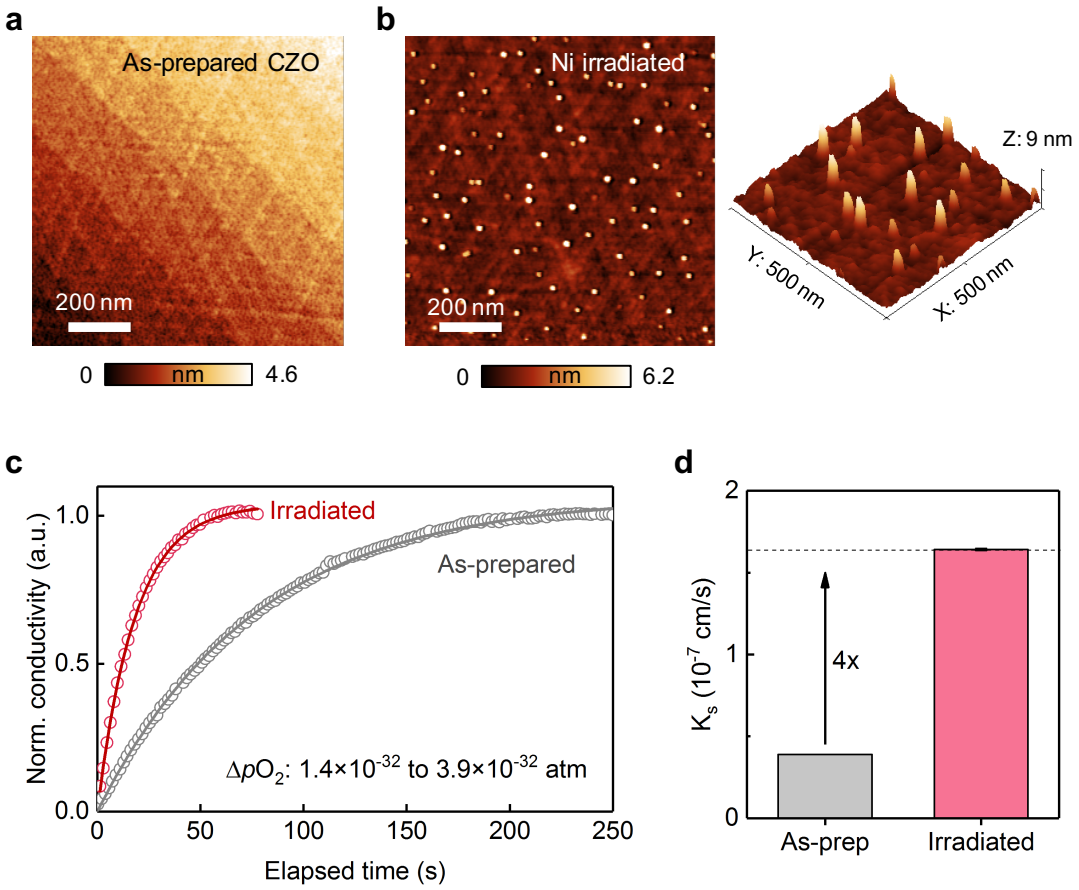

Figure S27. Ni irradiation on CeO_2-based materials systems. **(a-b)** AFM images of the 30 nm epitaxial (111)-oriented CZO film (a) before and (b) after 10 keV Ni irradiation. As illustrated, Ni irradiation decorated the CZO surface with well-dispersed nanoparticles. **(c)** Electrical conductivity relaxation profile of the CZO film with and without Ni irradiation at 400 °C in H_2/H_2O atmospheres. The solid lines represent exponential fitting profiles. **(d)** Comparison of the surface oxygen exchange coefficients (k_s) between the as-prepared and Ni-irradiated CZO. As illustrated, Ni irradiation increases the surface exchange kinetics of CZO by as much as four times. The dose for 10 keV Ni irradiation is 10^{15} cm^{-2}.

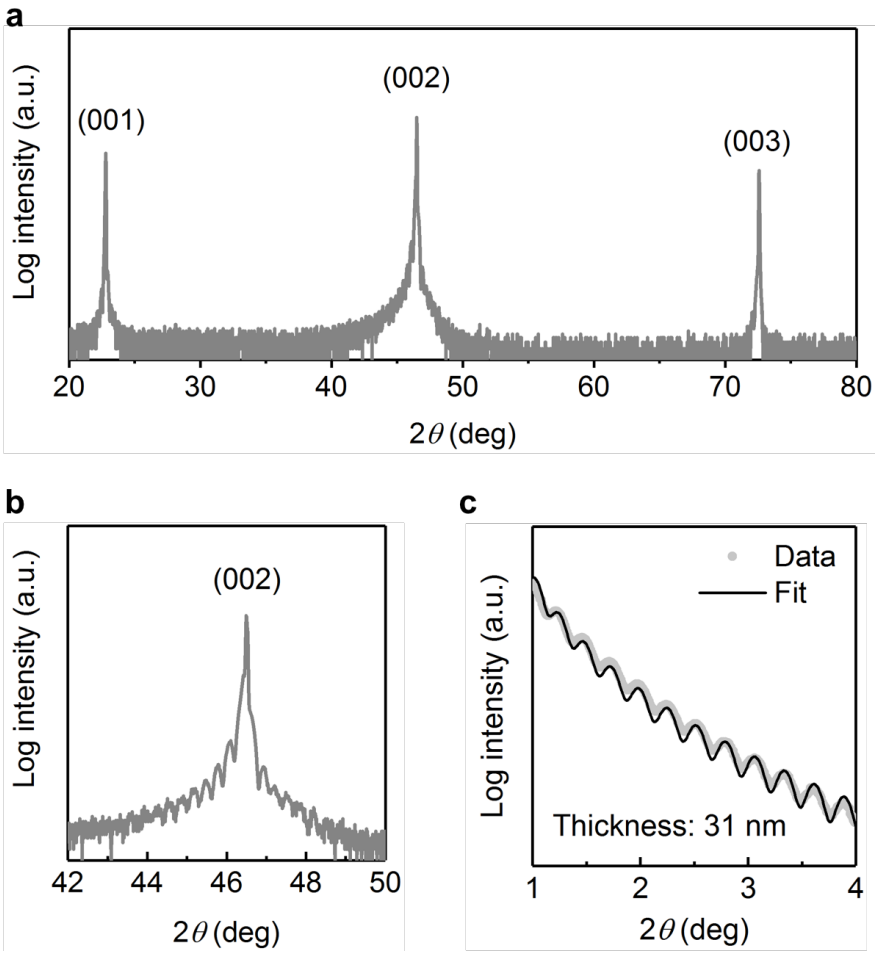

Figure S28. Structure analysis of the as-prepared STF film. (a) Out-of-plane θ-2θ X-ray diffraction pattern (XRD) of the as-prepared STF film shows the preferred (001) orientation. **(b)** High-resolution XRD around the (002) diffraction peak. Due to the similar lattice parameters, the XRD of the STF thin film overlaps with the Nb-doped $SrTiO_3$ substrate diffraction. Nevertheless, the presence of the epitaxial STF film can be confirmed by the Laue fringes. **(c)** X-ray reflectometry (XRR) from the as-prepared STF reveals a film thickness of 31 nm. Due to the similar electron densities between the STF film and the Nb-doped STO substrate, the XRR measurements were conducted on the STF film that is grown on the YSZ (001) substrate, using the same growth parameters as other samples used in this work.

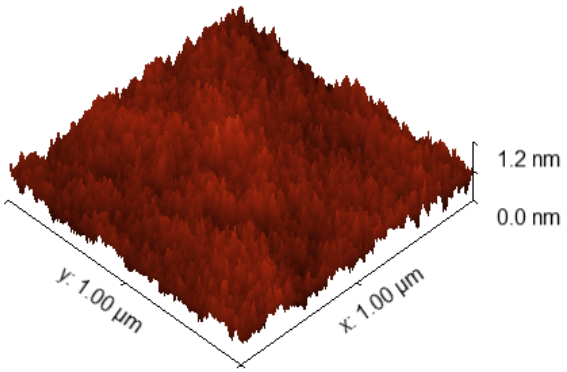

Figure S29. Atomic force microscopy (AFM) image of the as-prepared STF film. The root mean square surface roughness is 0.1 nm.

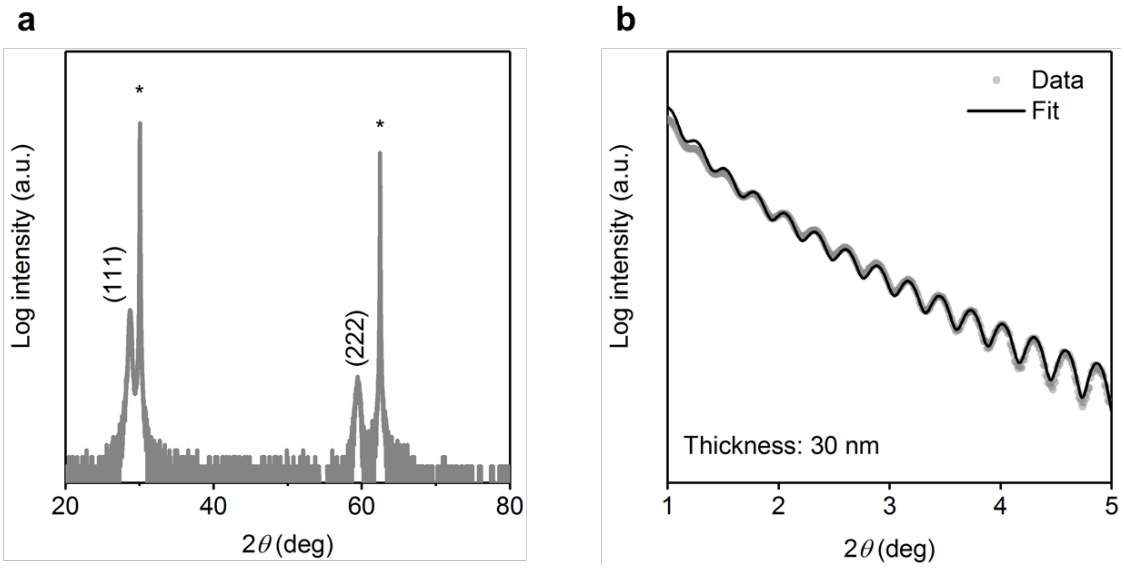

Figure S30. Structure characterization of the as-prepared CZO film. (a) Out-of-plane θ-2θ X-ray diffraction pattern (XRD) of the as-prepared CZO film shows the preferred (111) orientation. The diffraction patterns from the YSZ (111) substrate are labeled with asterisks. **(b)** X-ray reflectometry (XRR) from the as-prepared CZO reveals a film thickness of 30 nm.

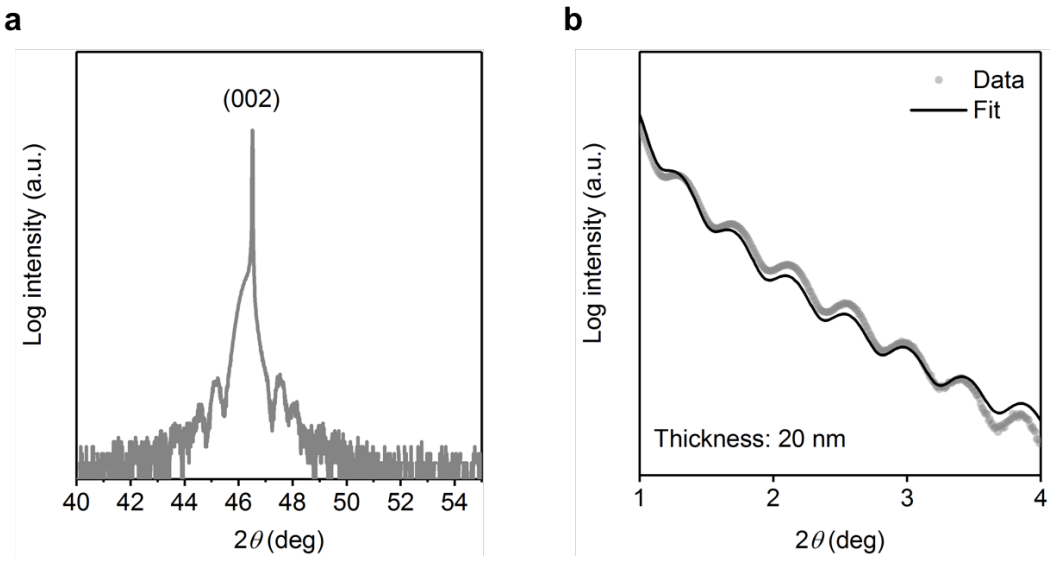

Figure S31. Structure characterization of the as-prepared LSF film. (a) Out-of-plane θ-2θ X-ray diffraction pattern (XRD) of the as-prepared LSF film around (002) diffraction peak. **(b)** X-ray reflectometry (XRR) from the as-prepared LSF reveals a film thickness of 20 nm.

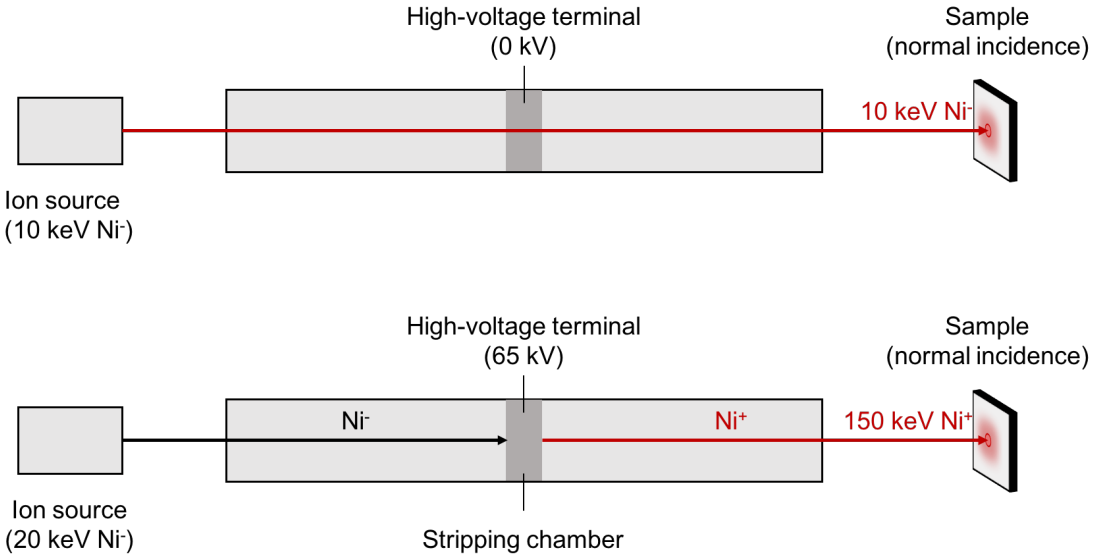

Figure S32. Methods to generate 10 keV Ni^- and 150 keV Ni^+ ion beams from the Tandem accelerator. For 10 keV Ni^- beam generation (top panel), the ion source was set to be 10 keV Ni^- and the high-voltage terminal was set to be 0 kV. In this configuration, the Tandem accelerator was operated as a collimator. For 150 keV Ni^+ beam, the ion source was set to be 20 keV Ni^-, and the high-voltage terminal was set to be 65 kV. The charge state of Ni ion is transformed from negative to positive at the voltage terminal. Then, after the two-step acceleration, we can obtain the 150 keV Ni^+ ions.

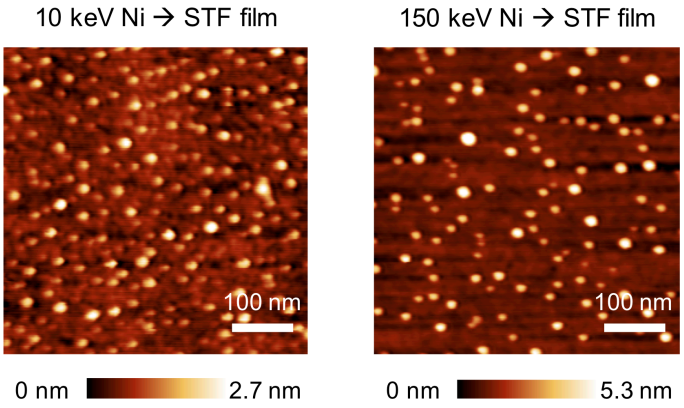

Figure S33. AFM images of the STF surfaces after Ni irradiation. No noticeable surface defects can be observed on the STF surface after both 10 KeV and 150 keV Ni irradiation. The irradiation dose is 5×10^{15} cm^{-2}.

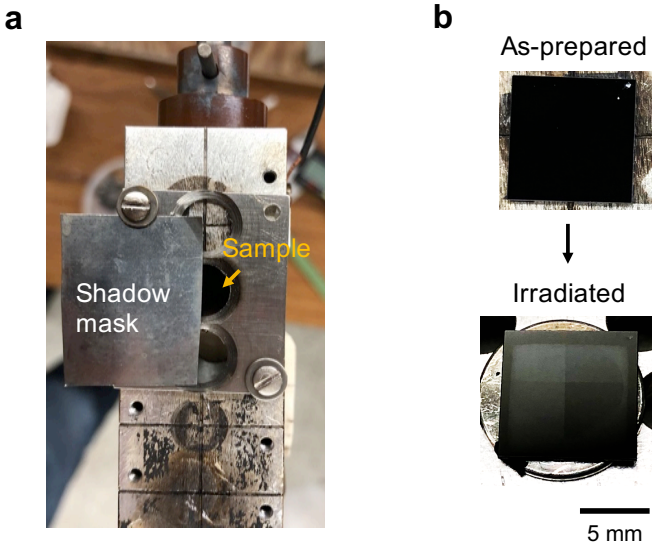

Figure S34. Spatially controlled irradiation. (a) Shadow mask used in the experiment. **(b)** Optical image of the LSF film before and after the spatially controlled irradiation, where the four differently irradiated regions (four quadrants) can be clearly visualized.

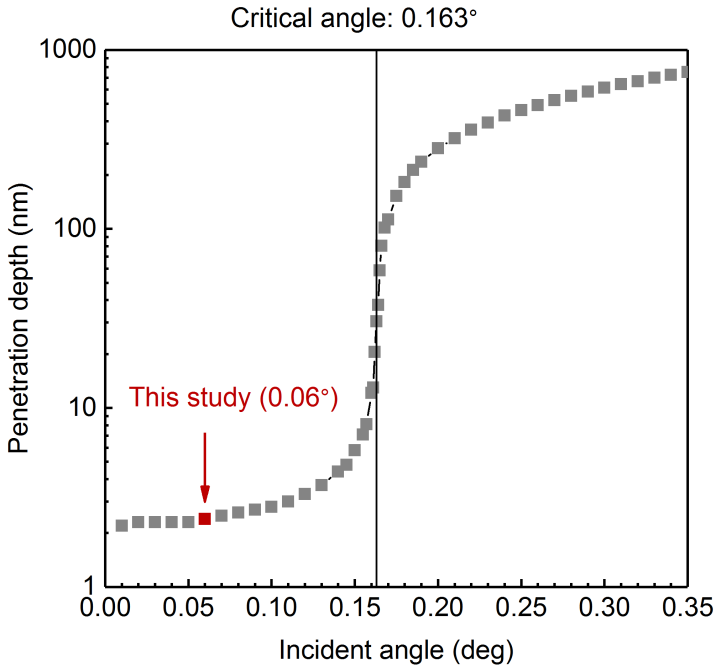

Figure S35. Penetration depth for the GID measurements. As illustrated, the critical angle for 15.5 keV X-ray in $SrTiO_3$ is 0.163 deg. In this study, we conducted GID measurements at an incident angle of 0.06 deg (indicated with arrow) to measure the surface structures. The energy-dependent X-ray penetration depth is calculated using the online tool box developed by the X-ray group at the Atominstitut of the TU Wien (https://gixa.ati.tuwien.ac.at/tools/penetrationdepth.xhtml). The density of the $SrTiO_3$ is set to be 4.81 g/cm^3 for the calculation.

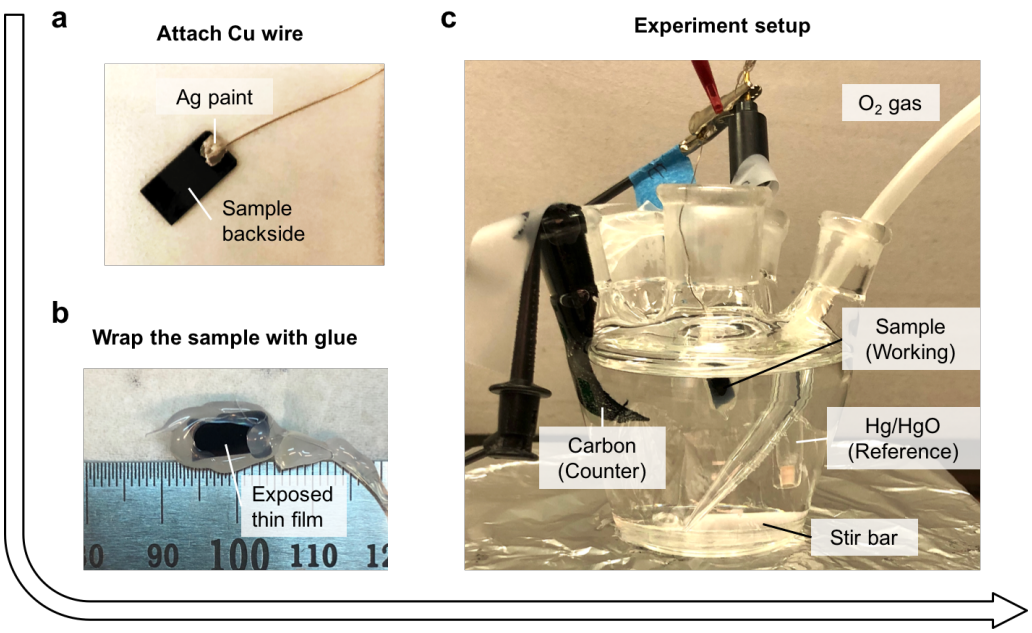

Figure S36. Experimental procedure for the OER measurement. (a) First, Cu wire was attached to the backside of the Nb:$SrTiO_3$ substrate using silver paint. **(b)** Secondly, the thin-film sample, together with the Cu wire, was encapsulated with hot glue to prevent direct contact to the electrolyte. **(c)** Finally, the OER experiment was conducted using the experimental setup shown in the image.

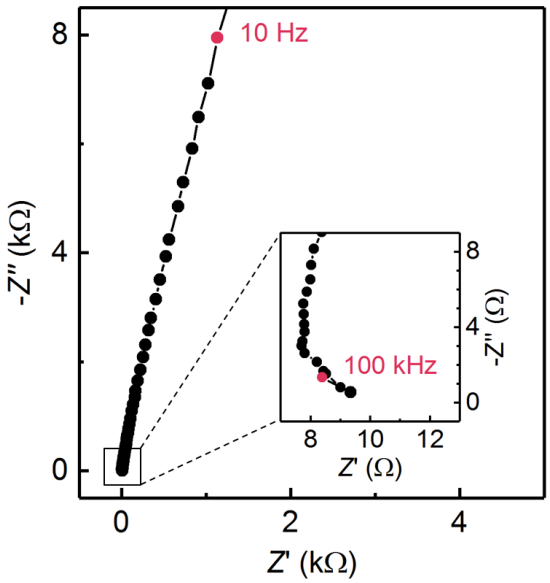

Figure S37. Representative electrochemical impedance spectroscopy (EIS) spectra of the STF film at OCV. As highlighted by the zoom-in plot, the ohmic resistance of the system is around 10 ohms.

References

1 Han, H. *et al*. Lattice strain-enhanced exsolution of nanoparticles in thin films. *Nature Communications* **10**, 1471 (2019). https://doi.org:10.1038/s41467-019-09395-4

2 Kyriakou, V. *et al*. Plasma Driven Exsolution for Nanoscale Functionalization of Perovskite Oxides. *Small Methods* **5**, 2100868 (2021). https://doi.org:https://doi.org/10.1002/smtd.202100868

3 Khalid, H. *et al*. Rapid Plasma Exsolution from an A-site Deficient Perovskite Oxide at Room Temperature. *Advanced Energy Materials* **12**, 2201131 (2022). https://doi.org:https://doi.org/10.1002/aenm.202201131

4 Sun, Z., Fan, W. & Bai, Y. A Flexible Method to Fabricate Exsolution-Based Nanoparticle-Decorated Materials in Seconds. *Advanced Science* **9**, 2200250 (2022). https://doi.org:https://doi.org/10.1002/advs.202200250

5 Myung, J.-h., Neagu, D., Miller, D. N. & Irvine, J. T. S. Switching on electrocatalytic activity in solid oxide cells. *Nature* **537**, 528-531 (2016). https://doi.org:10.1038/nature19090

6 Opitz, A. K. *et al*. Understanding electrochemical switchability of perovskite-type exsolution catalysts. *Nature Communications* **11**, 4801 (2020). https://doi.org:10.1038/s41467-020-18563-w

7 Fan, W. *et al*. Anodic Shock-Triggered Exsolution of Metal Nanoparticles from Perovskite Oxide. *Journal of the American Chemical Society* **144**, 7657-7666 (2022). https://doi.org:10.1021/jacs.1c12970

8 Kim, H. *et al*. Unveiling the key factor for the phase reconstruction and exsolved metallic particle distribution in perovskites. *Nature Communications* **12**, 6814 (2021). https://doi.org:10.1038/s41467-021-26739-1

9 Tsiotsias, A. I. *et al*. Bimetallic Exsolved Heterostructures of Controlled Composition with Tunable Catalytic Properties. *ACS Nano* **16**, 8904-8916 (2022). https://doi.org:10.1021/acsnano.1c11111

10 Weber, M. L. *et al*. Exsolution of Embedded Nanoparticles in Defect Engineered Perovskite Layers. *ACS Nano* **15**, 4546-4560 (2021). https://doi.org:10.1021/acsnano.0c08657

11 Guo, J. *et al*. Low-Temperature Exsolution of Ni–Ru Bimetallic Nanoparticles from A-Site Deficient Double Perovskites. *Small* **18**, 2107020 (2022). https://doi.org:https://doi.org/10.1002/smll.202107020

12 Horlick, S. A., Huang, Y.-L., Robinson, I. A. & Wachsman, E. D. Controlling exsolution with a charge-balanced doping approach. *Nano Energy* **87**, 106193 (2021). https://doi.org:https://doi.org/10.1016/j.nanoen.2021.106193

13 Oh, J. *et al*. Precise Modulation of Triple-Phase Boundaries towards Highly Functional Exsolved Catalyst for Dry Reforming of Methane under A Dilution-Free System. *Angewandte Chemie International Edition* **61**, e202204990 (2022). https://doi.org:https://doi.org/10.1002/anie.202204990

14 Li, Y. *et al*. Perovskite-Socketed Sub-3 nm Copper for Enhanced CO2 Electroreduction to C2+. *Advanced Materials* **34**, 2206002 (2022). https://doi.org:https://doi.org/10.1002/adma.202206002

15 Chen, Z. *et al*. Organic Photochemistry-Assisted Nanoparticle Segregation on Perovskites. *Cell Reports Physical Science*, 100243 (2020). https://doi.org:https://doi.org/10.1016/j.xcrp.2020.100243

16 Shin, E. *et al*. Ultrafast Ambient-Air Exsolution on Metal Oxide via Momentary Photothermal Effect. *ACS Nano* (2022). https://doi.org:10.1021/acsnano.2c05128

17 Joo, S. *et al*. Cation-swapped homogeneous nanoparticles in perovskite oxides for high power density. *Nature Communications* **10**, 697 (2019). https://doi.org:10.1038/s41467-019-08624-0

18 Kim, J. K. *et al*. Exceptional Tunability over Size and Density of Spontaneously Formed Nanoparticles via Nucleation Dynamics. *ACS Applied Materials & Interfaces* **12**, 24039-24047 (2020). https://doi.org:10.1021/acsami.0c05215

19 López-García, A. *et al*. Tuning Ternary Alloyed Nanoparticle Composition and Morphology by Exsolution in Double Perovskite Electrodes for CO2 Electrolysis. *ACS Applied Energy Materials* **5**, 13269-13283 (2022). https://doi.org:10.1021/acsaem.2c01829

20 Lv, H. *et al*. Promoting exsolution of RuFe alloy nanoparticles on Sr2Fe1.4Ru0.1Mo0.5O6–δ via repeated redox manipulations for CO2 electrolysis. *Nature Communications* **12**, 5665 (2021). https://doi.org:10.1038/s41467-021-26001-8

21 Nečas, D. & Klapetek, P. Gwyddion: an open-source software for SPM data analysis. *Open Physics* **10**, 181-188 (2012). https://doi.org:doi:10.2478/s11534-011-0096-2

22 Zimicz, M. G., Prado, F. D., Lamas, D. G. & Larrondo, S. A. In-situ XANES and XPD studies of NiO/Ce0.9Zr0.1O2 IT-SOFCs anode nanomaterial as catalyst in the CPOM reaction. *Applied Catalysis A: General* **542**, 296-305 (2017). https://doi.org:https://doi.org/10.1016/j.apcata.2017.05.040

23 Yu, M., Moon, G., Bill, E. & Tüysüz, H. Optimizing Ni–Fe Oxide Electrocatalysts for Oxygen Evolution Reaction by Using Hard Templating as a Toolbox. *ACS Applied Energy Materials* **2**, 1199-1209 (2019). https://doi.org:10.1021/acsaem.8b01769

24 Gopal, C. B. & Haile, S. M. An electrical conductivity relaxation study of oxygen transport in samarium doped ceria. *Journal of Materials Chemistry A* **2**, 2405-2417 (2014). https://doi.org:10.1039/C3TA13404K